Ultrafast modification of Hubbard U in a strongly correlated material: *ab initio* high-harmonic generation in NiO

Nicolas Tancogne-Dejean,[1,*] Michael A. Sentef,[1] and Angel Rubio[1,2,3,†]

[1] *Max Planck Institute for the Structure and Dynamics of Matter and Center for Free-Electron Laser Science, Luruper Chaussee 149, 22761 Hamburg, Germany*

[2] *Nano-Bio Spectroscopy Group and ETSF, Universidad del País Vasco, , 20018 San Sebastián, Spain*

[3] *Center for Computational Quantum Physics (CCQ), The Flatiron Institute, 162 Fifth Avenue, New York NY 10010*

DEPENDENCE OF U IN GROUND-STATE OCCUPATIONS

In order to show that the change in U is linked to the change in orbital occupations, we also performed DFT+U calculations with constrained occupations. We employed a coarser $14 \times 14 \times 7$ **k**-point grid for these calculations, as we are not interesting in converging the HHG spectra.

In order to constrain the occupations, we follow the approached developed in Refs. [1, 2], in which the constrain of the occupations of the localized orbitals is performed by adding a localized potential with a weight α. Here we do not use this approach to determine the value of U from a LDA calculation, but we rather use it together with the ACBN0 functional, such that the potential given by Eq.(2) in the main text becomes

$$\hat{\tilde{V}}^{\sigma}_{U}[n,\{n^{\sigma}_{mm'}\}] = \hat{V}^{\sigma}_{U}[n,\{n^{\sigma}_{mm'}\}] + \alpha P^{\sigma}_{m,m}\,. \qquad (1)$$

We implemented this method in the Octopus code [3]. For each value of α, we first performed a ground-state calculation with the ACBN0 functional. Then we added the constrain α and performed again a fully self-consistent calculation, such that the system can adapt to the perturbation. Our analysis, summarized in Fig. 1 shows that the change in U_{eff} is directly controlled by the constrained α, which constrains properly the occupations (see right panel of Fig. 1). This ground-state analysis confirm that the variation of U_{eff} depends on the occupation of the localized orbitals.

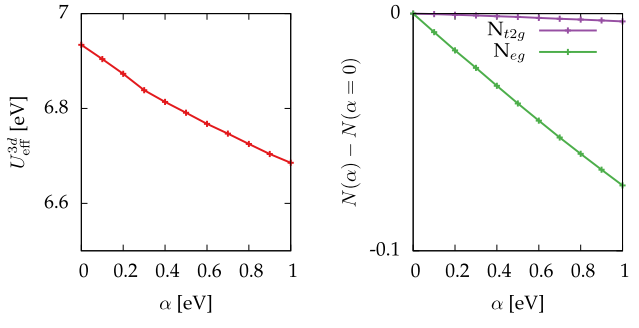

Supplementary Fig. 1. Effective on-site U for the 3d orbitals of Ni (left panel) and occupations of these orbitals (right panel) *versus* the constrained α.

POPULATION ANALYSIS OF THE LOCALIZED ORBITALS

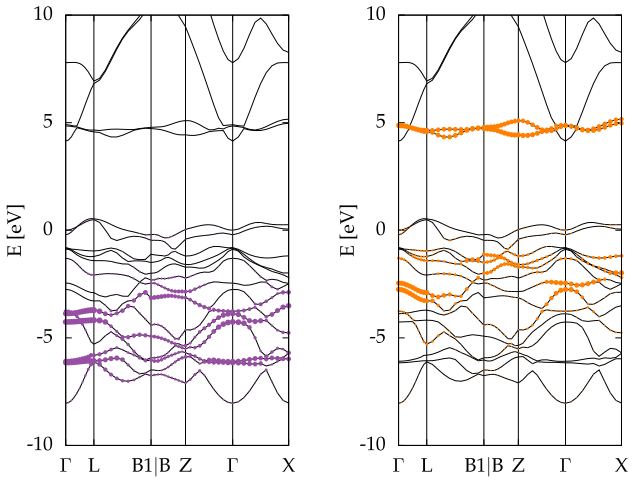

Supplementary Fig. 2. $3d$ orbital character for the first Ni atom for spin up (left) and spin down (right). The size of the dots indicates the orbital character.

By taking the diagonal elements of the density matrix of the localized subspace n^{σ}, we have access to the population of the localized orbitals with respect to time. Our results, shown in Fig. 3 and Fig. 4 are only reported for one atom, as the other atom gives the same results, but with an opposite spin (due to the antiferromagnetic order).

Even at the higher intensity considered in the main text (used in Fig. 3 and Fig. 4), we do not observe the saturation of the population on a time-scale of 20fs, in opposition to what is observed for the time-dependent U. Our results are found to be fully compatible with the excitation by a laser. The $2p$ populations decrease, and behave the same for each atom, as the oxygen atoms are not spin-polarized. For the Ni atoms we found that the population of the $t2g$ orbitals, which are initially fully occupied ($N_{t2g}(t_0) \sim 3$), decreases with time. This is

also true for the *eg* orbitals for spin up, but as these orbitals are further away from the Fermi energy, thus the population of the orbitals is less affected by the laser. On the other side, the population of the *eg* orbitals for spin down, which correspond mainly to the almost flat conduction band, is found to increase while we are injecting electrons in the conduction bands.

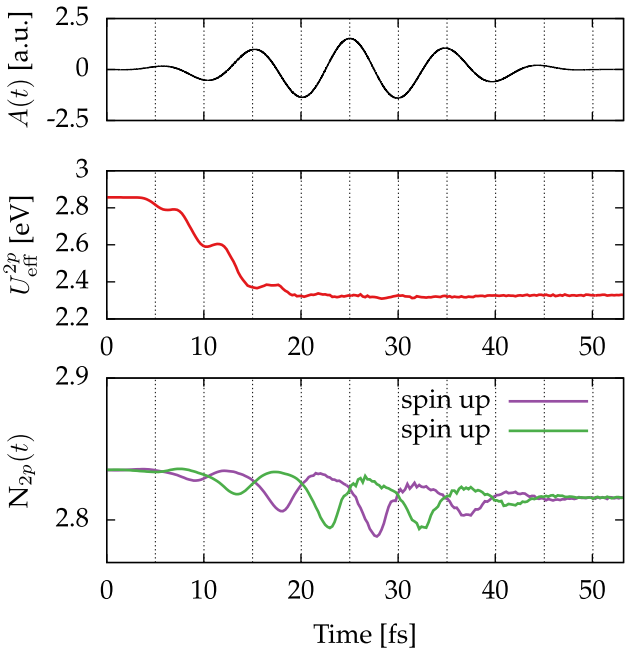

Supplementary Fig. 3. Time evolution of the U for the $2p$ orbitals for the first O atom (middle panel) and the corresponding orbital occupations (bottom panel), for the driving vector potential (top panel) with an intensity of $I_0 = 5 \times 10^{12}\,\mathrm{W\,cm^{-2}}$.

The quick saturation of U is explained by the change of the on-site screening, as explained in the next section.

ON-SITE SCREENING AND SATURATION OF THE TIME-DEPENDENT U

In order to understand more deeply the physical mechanism leading to a saturation in the change of U, we analyze here the one-site screening which is included in the ACBN0 functional [4].

In the ACBN0 functional, the electron-electron interaction which is added to the DFT Hamiltonian is

$$E_{ee} = \frac{1}{2}\sum_{\{m\}}\sum_{\alpha,\beta}\bar{P}^{\alpha}_{mm'}\bar{P}^{\beta}_{m''m'''}(mm'|m''m''') - \frac{1}{2}\sum_{\{m\}}\sum_{\alpha}\bar{P}^{\alpha}_{mm'}\bar{P}^{\alpha}_{m''m'''}(mm'''|m''m')\,, \quad (2)$$

In Eq. 2, the renormalized occupation matrices $\bar{P}^{I,n,l,\sigma}_{mm'}$ and the renormalized occupations $\bar{N}^{I,n,l,\sigma}_{\psi_{n\mathbf{k}}}$ are respectively given by [4]

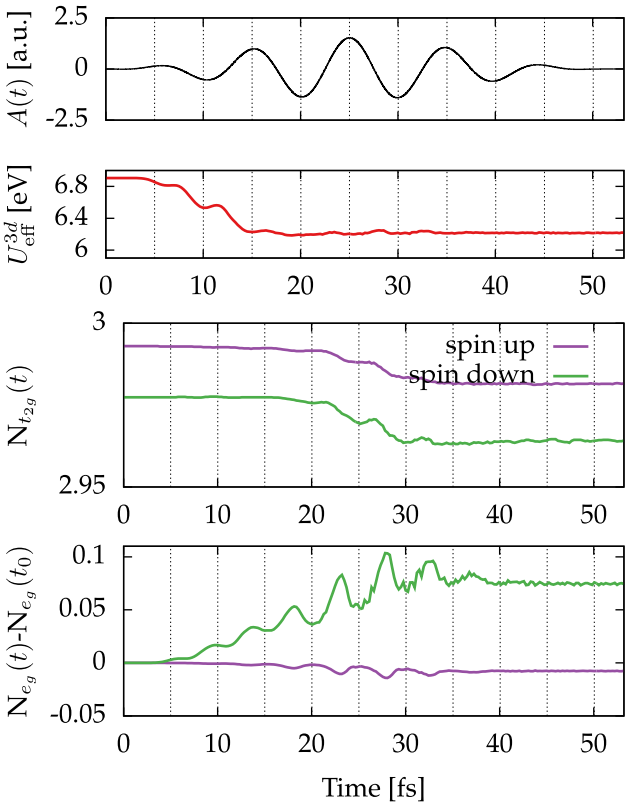

Supplementary Fig. 4. Same as in Fig. 3, but for the $3d$ orbitals of Ni. Here we considered separately the *eg* and $t2g$ orbitals. The *eg* orbitals for spin up are initially fully occupied, and the ones for spin down are initially not occupied, in agreement with the orbital-resolved bandstructure shown in Fig. 2.

$$\bar{P}^{I,n,l,\sigma}_{mm'} = \sum_{n\mathbf{k}} w_{\mathbf{k}} f_{n\mathbf{k}} \bar{N}^{I,n,l,\sigma}_{\psi_{n\mathbf{k}}} \langle\psi^{\sigma}_{n\mathbf{k}}|\phi_{I,n,l,m}\rangle\langle\phi_{I,n,l,m'}|\psi^{\sigma}_{n\mathbf{k}}\rangle\,, \quad (3)$$

$$\bar{N}^{I,n,l,\sigma}_{\psi_{n\mathbf{k}}} = \sum_{\{I\}}\sum_{m}\langle\psi^{\sigma}_{n\mathbf{k}}|\phi_{I,n,l,m}\rangle\langle\phi_{I,n,l,m}|\psi^{\sigma}_{n\mathbf{k}}\rangle\,, \quad (4)$$

where I is an atom and n, l and m are the quantum number defining the localized orbitals. These subscripts are omitted below for conciseness.

The key idea of the ACBN0 functional is to define U and J by comparing Eq. 2 with the usual expression of DFT+U,

$$E_{ee}[\{n^{I,\sigma}_{mm'}\}] = \frac{U}{2}\sum_{m,m',\sigma} N^{\sigma}_{m} N^{-\sigma}_{m'} + \frac{U-J}{2}\sum_{m\neq m',\sigma} N^{\sigma}_{m} N^{\sigma}_{m'}\,. \quad (5)$$

Doing this, one obtains the ab initio U and J of the ACBN0 functional

$$\bar{U} = \frac{\sum_{\{m\}}\sum_{\alpha\beta}\bar{P}^{\alpha}_{mm'}\bar{P}^{\beta}_{m'm''}(mm'|m''m''')}{\sum_{m\neq m'}\sum_{\alpha}N^{\alpha}_{m}N^{\alpha}_{m'} + \sum_{\{m\}}\sum_{\alpha}N^{\alpha}_{m}N^{-\alpha}_{m'}}\,, \quad (6)$$

$$\bar{J} = \frac{\sum_{\{m\}} \sum_{\alpha} \bar{P}^{\alpha}_{mm'} \bar{P}^{\alpha}_{m'm''}(mm'''|m''m')}{\sum_{m \neq m'} \sum_{\alpha} N^{\alpha}_{m} N^{\alpha}_{m'}}, \quad (7)$$

with $N^{\alpha}_{m} = n^{I,n,l,\alpha}_{mm}$. This are these expressions that are evaluated in the present work.

However, we can take a different point of view. Eq. 2 could be compared to another expression, which is the one that would be used if one would compute the screened Coulomb matrix $U_{mm'm''m'''}$

$$E_{ee} = \frac{1}{2} \sum_{\{m\}} \sum_{\alpha,\beta} n^{\alpha}_{mm'} n^{\beta}_{m''m'''} U_{mm'm''m'''} - \frac{1}{2} \sum_{\{m\}} \sum_{\alpha} n^{\alpha}_{mm'} n^{\alpha}_{m''m'''} U_{mm'''m''m'}, \quad (8)$$

In this expression, the U matrix is evaluated computing the matrix elements of the dynamical screened Coulomb interaction $W(\omega) = \epsilon^{-1}(\omega)v$, where v is the unscreened Coulomb interaction, and $\epsilon^{-1}(\omega)$ is the inverse of the dynamical dielectric screening experience by the electrons in the localized subspace. This is what would be evaluated for instance using the cRPA method [5–8].

We now define the effective on-site screening which is taken into account in our simulations. For this, we start from Eq. 8 in which we make explicit the screened Coulomb interaction.

$$E_{ee} = \frac{1}{2} \sum_{\{m\}} \sum_{\alpha,\beta} n^{\alpha}_{mm'} n^{\beta}_{m''m'''} \langle mm''|W(\omega)|m'm'''\rangle - \frac{1}{2} \sum_{\{m\}} \sum_{\alpha} n^{\alpha}_{mm'} n^{\alpha}_{m''m'''} \langle mm''|W(\omega)|m'''m'\rangle, \quad (9)$$

where

$$\langle mm''|W(\omega)|m'm'''\rangle = \int d^3\mathbf{r} \int d^3\mathbf{r}' \epsilon^{-1}(\mathbf{r},\mathbf{r}',\omega) \times \frac{\phi^{\dagger}_{m}(\mathbf{r})\phi^{\dagger}_{m''}(\mathbf{r}')\phi_{m'}(\mathbf{r})\phi_{m'''}(\mathbf{r}')}{|\mathbf{r}-\mathbf{r}'|}.$$

By omitting the dynamical features of the screened Coulomb interaction, and further assuming the screening can be approximated by an effective on-site screening, i.e., averaged spatially on the correlated subspace, we obtain

$$E_{ee} = \frac{1}{2} \sum_{\{m\}} \sum_{\alpha,\beta} n^{\alpha}_{mm'} n^{\beta}_{m''m'''} \epsilon^{-1}_{\text{eff}} \langle mm''|v|m'm'''\rangle - \frac{1}{2} \sum_{\{m\}} \sum_{\alpha} n^{\alpha}_{mm'} n^{\alpha}_{m''m'''} \epsilon^{-1}_{\text{eff}} \langle mm''|v|m'''m'\rangle.$$

By comparing this expression to Eq. 2, we arrive to the definition of the effective on-site screening taking into account in the ACBN0 functional as

$$\epsilon^{-1}_{\text{eff}} = \frac{\bar{P}^{\alpha}_{mm'} \bar{P}^{\beta}_{m''m'''}}{n^{\alpha}_{mm'} n^{\beta}_{m''m'''}}. \quad (10)$$

In this expression, the effective screening appears as spin and orbital dependent. However we checked that computing the effective screening for the different orbitals yields very similar results for each orbitals, as expected. In Fig. 5 and Fig. 6, we report the time-evolution of the effective on-site screening for the $3d$ orbitals and the $2p$ orbitals, computing by taking the average over the orbitals and spin channels of Eq. 10.

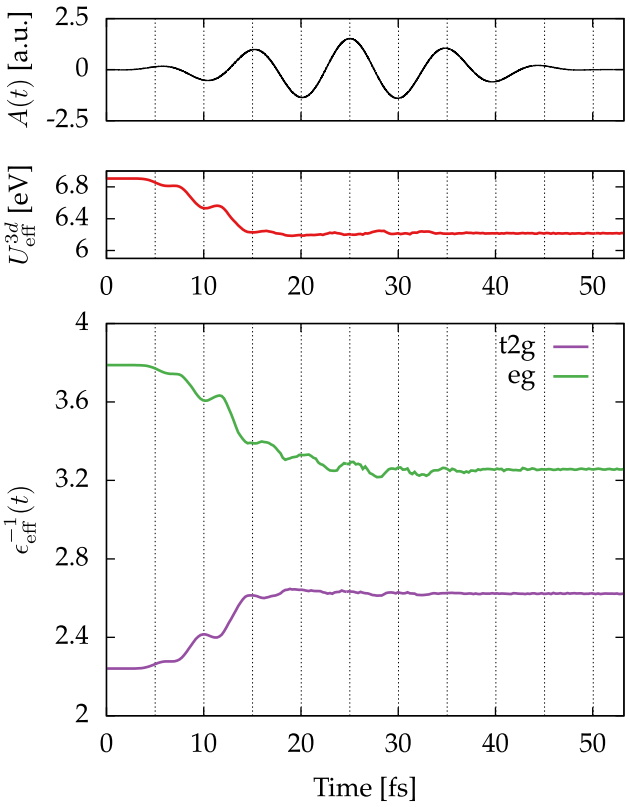

Supplementary Fig. 5. Time-evolution of the effective on-site screening for the $t2g$ and eg orbitals of the Ni atoms (bottom panel), compared to the laser field (top panel) and the time-dependent U_{eff}. See the main text for details

We obtained that the effective on-site screening is quite different of the $t2g$ and eg orbitals. From the population analysis above, we found that the laser depletes the $t2g$ orbitals and increases the population in the eg orbitals for the spin down channel. The spin-up channel for the eg, the population mostly does not change, as these orbitals are deeper in energy. The changes obtained for the on-site screening are fully compatible with the previous population analysis. We obtain in particular that the time-scale on which U changes is dictated by the effective on-site screening of the $t2g$ orbitals, which are the most relevant orbitals here, as they are fully occupied in the ground state. Note that the eg on-site screening is found to change on the same time-scale as the laser pulse or the orbital occupations.

For the $2p$ orbitals, we obtained that the on-site effec-

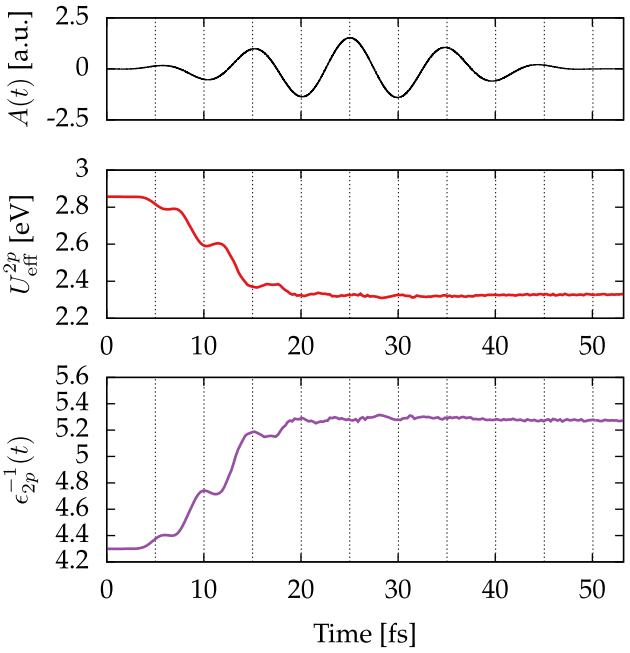

Supplementary Fig. 6. Time-evolution of the effective on-site screening for the $2p$ orbitals of the O atoms (bottom panel), compared to the laser field (top panel) and the time-dependent $U_{\rm eff}$.

tive screening is also changing on the same time-scale as the on-site $U_{\rm eff}$.

To summarize our findings, we found that the time-scale on which the on-site effective screening evolves and then saturates is the same as for the on-site $U_{\rm eff}$, explaining the reported saturation of U at high field strength.

COMPARISON OF HHG SPECTRUM OF NIO FOR PBE AND ACBN0 FUNCTIONAL

We computed the HHG spectrum of NiO from the PBE functional [9] compared to the ACBN0 functional [4] as used in the main text. Due to the smaller band-gap predicted by PBE, we used a much smaller intensity of $I_0 = 1\times10^{11}\mathrm{W\,cm^{-2}}$. As shown in Fig. 7, the HHG from NiO is clearly overestimated, as the gap is much smaller (1.26eV for PBE compared to 4.14 eV with ACBN0 functional, the latter been very close to the experimental one [10]).

HHG SPECTRA WITH AND WITHOUT TIME-DEPENDENT U FOR VARIOUS INTENSITIES

We also report the HHG spectrum of NiO for lower intensity ($I_0 = 5\times10^{11}\mathrm{W\,cm^{-2}}$, Fig. 8) and higher intensity ($I_0 = 5\times10^{12}\mathrm{W\,cm^{-2}}$, Fig. 10) which also shows

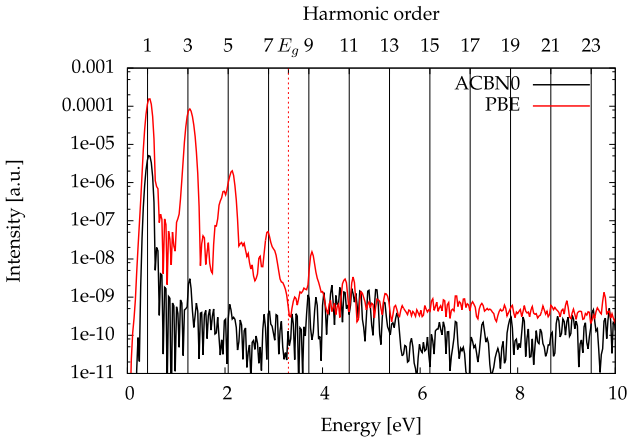

Supplementary Fig. 7. Comparison of the HHG from NiO for PBE (red line) and ACBN0 (black line) functional for $I_0 = 1\times10^{11}\mathrm{W\,cm^{-2}}$.

that freezing the Hubbard U underestimate the harmonic yield.

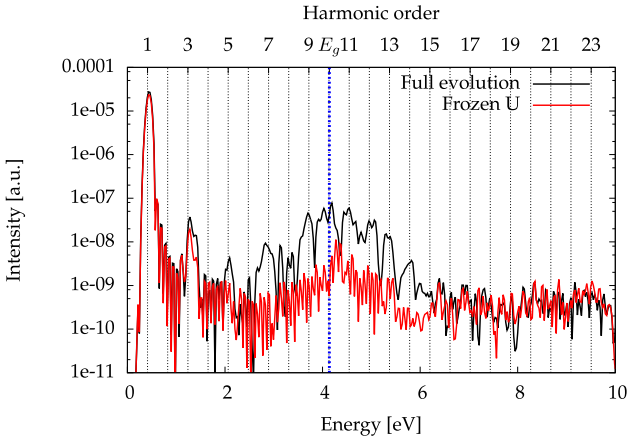

Supplementary Fig. 8. Effect of the time-evolution of the effective Hubbard U on the HHG spectrum of NiO. The HHG spectrum obtained from the full time-evolution is shown in black, whereas the spectra obtained when fixing the Hubbard U to its ground-state value is shown in red. The red vertical line indicates the calculated band-gap of NiO. The intensity is taken here as $I_0 = 5\times10^{11}\mathrm{W\,cm^{-2}}$.

EFFECT OF THE PULSE LENGTH ON THE DECREASE OF U

It is important to note that the dynamics of U not only depends on the intensity, but also depends on the shape and the length of the applied laser pulse. As an example, we obtained that a shorter pulse of 12.5fs yield a reduction of U of 0.53eV instead of 0.58eV for 25fs (see Fig.2 in the main text), for the same intensity of

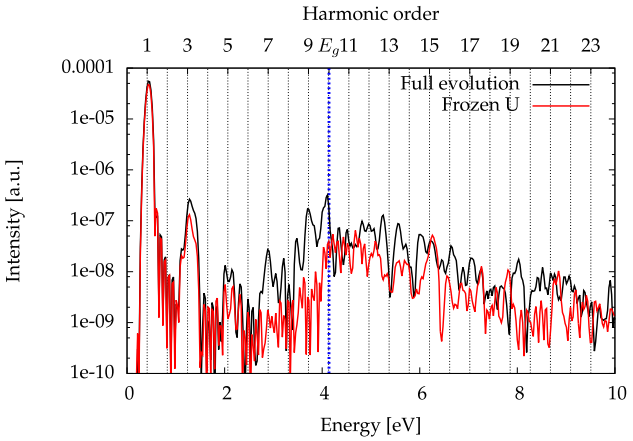

Supplementary Fig. 9. Same as Fig. 8 but with $I_0 = 1 \times 10^{12}\mathrm{W\,cm^{-2}}$

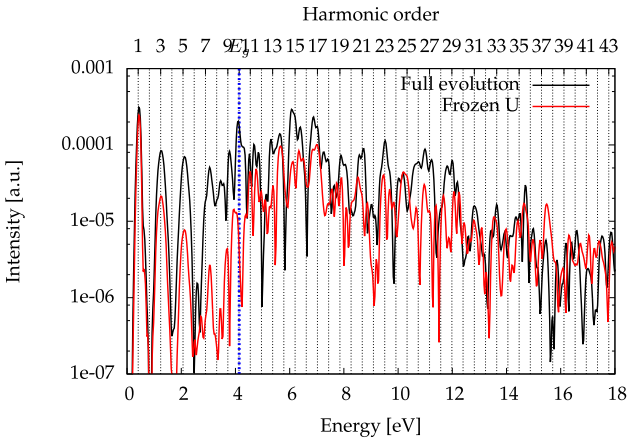

Supplementary Fig. 10. Same as Fig. 8 but with $I_0 = 5 \times 10^{12}\mathrm{W\,cm^{-2}}$

$I_0 = 5 \times 10^{11}\mathrm{W\,cm^{-2}}$.

EFFECT OF DYNAMICAL U ON LOW-ORDER SUSCEPTIBILITIES

One interesting question is how much the low-order susceptibilities are affected by the dynamical U and how much they change compared to the intensity of the driving field. As the main purpose of our paper is not to calculate these susceptibilities, we cannot extract precise values from our simulations. This would require longer time propagations to make the finite pulse-length effect less important. However, we can still extract some values from the simulations, to discuss a general trend and compare with available experimental values for the third-order susceptibilities χ^3. In order to evaluate the first- and third-order susceptibilities from our simulations, we follow the method proposed in Ref. [11], and we assume

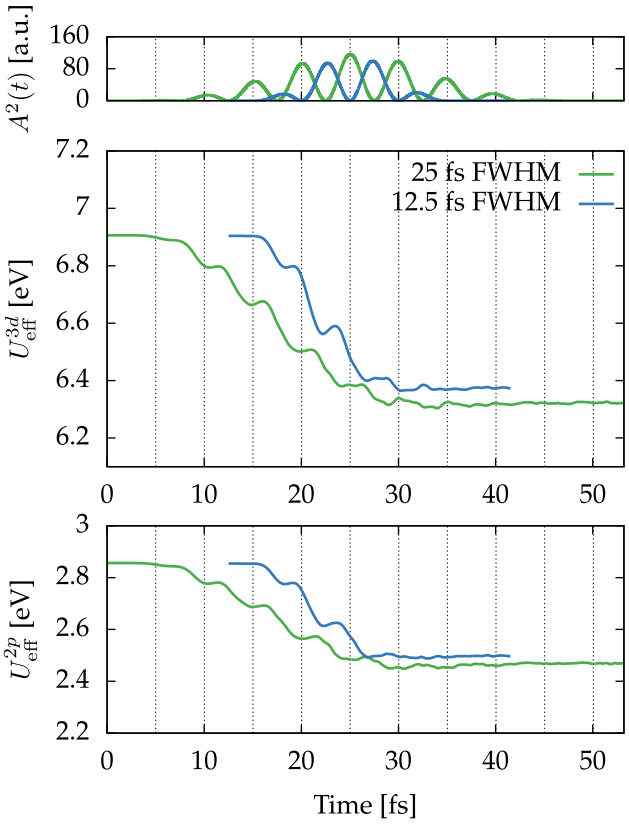

Supplementary Fig. 11. Self-consistent dynamics of Hubbard U for the Ni $3d$ orbitals (top panel), and the oxygen $2p$ orbitals (bottom panel) for different pulse length as indicated. The intensity is taken here as $I_0 = 5 \times 10^{11}\mathrm{W\,cm^{-2}}$.

a quasi-chromatic driving field F_δ, sharply peaked at a central frequency $\omega_0 = 0.43$eV. This is an assumption which is not fully fulfilled here, as only ultrashort driving pulses are considered.

The third order polarization is given (for three fields along the same direction) by [11]

$$P^{(3)}(3\omega_0) \approx \chi^{(3)}(-3\omega_0;\omega_0,\omega_0,\omega_0) \times \int_{-w_c}^{w_c} \frac{d\omega' d\omega''}{(2\pi)^2} F_\delta(w_0 - w' - w'') F_\delta(w_0 + w') F_\delta(w_0 + w''). \tag{11}$$

Assuming no intraband currents, we can link the polarization to the electronic current by

$$\begin{aligned} j^{(3)}(3\omega_0) &= 3i\omega_0 P^{(3)}(3\omega_0) \\ &= 3i\omega_0 \chi^{(3)}(-3\omega_0;\omega_0,\omega_0,\omega_0) F^{(3)}_{\mathrm{eff}}, \end{aligned}$$

where $F^{(3)}_{\mathrm{eff}}$ refers to the double integral in Eq. 11.

The assumption of no intraband current is clearly here a strong approximation, as we consider strong driving fields. However, going beyond this approximation for the evaluation of χ^3 and clearly splitting the contribution to the electronic current into interband and intraband contributions goes beyond the scope of the present work.

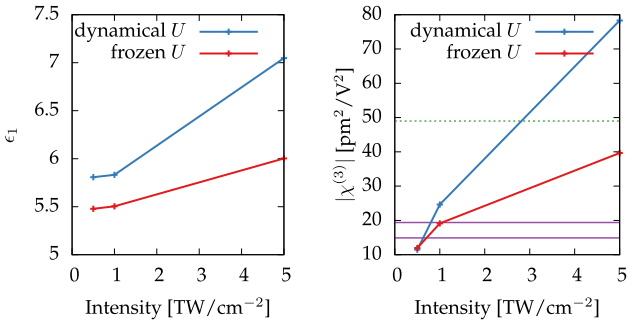

Supplementary Fig. 12. Extracted effective dielectric function (left panel) and third-order susceptibility (right panel) *versus* driver intensity. For evaluating χ^3, we used $\omega_c \approx 0.14$ eV and we checked that changing this value to a larger one does not affect significantly the extracted values. The experimental values are indicated by horizontal lines on the right panel, see main text for details.

In Fig. 12 we show the extracted effective dielectric function (left panel) and third-order susceptibility (right panel) *versus* driver intensity. As expected, in the low intensity region, the frozen and dynamical U results agrees well, whereas the difference becomes more and more important while intensity increases. For the third-order susceptibility, our result ($1.07m^2/V^2$ for an intensity of 10^{11}W/cm^2) seem to agree reasonably well with experimental values taken from Ref. [12] (horizontal solid lines, 1.49m^2/V^2 and 1.94m^2/V^2) and from [13] (horizontal dashed lines, 4.9m^2/V^2), showing that our TDDFT+U calculation can yield reasonably good values for third-harmonic generation. Performing the same estimate for the PBE calculation shown in Fig. 7 yield a value of $\chi^{(3)}(-3\omega_0;\omega_0,\omega_0,\omega_0)$ two orders of magnitude larger, due to the much smaller gap given by PBE. We found that for lower intensities, no reliable χ^3 can be extracted, as the pulse length is too short to lead to sizable third-harmonic generation.

Supplementary References

* nicolas.tancogne-dejean@mpsd.mpg.de
† angel.rubio@mpsd.mpg.de

[1] W. E. Pickett, S. C. Erwin, and E. C. Ethridge, Phys. Rev. B **58**, 1201 (1998).
[2] M. Cococcioni and S. de Gironcoli, Phys. Rev. B **71**, 035105 (2005).
[3] X. Andrade, D. Strubbe, U. De Giovannini, A. H. Larsen, M. J. T. Oliveira, J. Alberdi-Rodriguez, A. Varas, I. Theophilou, N. Helbig, M. J. Verstraete, L. Stella, F. Nogueira, A. Aspuru-Guzik, A. Castro, M. A. L. Marques, and A. Rubio, Phys. Chem. Chem. Phys. **17**, 31371 (2015).
[4] L. A. Agapito, S. Curtarolo, and M. Buongiorno Nardelli, Physical Review X **5**, 011006 (2015).
[5] T. Miyake and F. Aryasetiawan, Physical Review B **77**, 085122 (2008).
[6] M. Aichhorn, L. Pourovskii, V. Vildosola, M. Ferrero, O. Parcollet, T. Miyake, A. Georges, and S. Biermann, Physical Review B **80**, 085101 (2009).
[7] T. Miyake, F. Aryasetiawan, and M. Imada, Physical Review B **80**, 155134 (2009).
[8] M. Aichhorn, S. Biermann, T. Miyake, A. Georges, and M. Imada, Physical Review B **82**, 064504 (2010).
[9] J. P. Perdew, K. Burke, and M. Ernzerhof, Physical review letters **77**, 3865 (1996).
[10] N. Tancogne-Dejean, M. J. T. Oliveira, and A. Rubio, Physical Review B **96**, 245133 (2017).
[11] Y. Takimoto, F. D. Vila, and J. J. Rehr, The Journal of Chemical Physics **127**, 154114 (2007), https://doi.org/10.1063/1.2790014.
[12] T. Chtouki, L. Soumahoro, B. Kulyk, H. Bougharraf, B. Kabouchi, H. Erguig, and B. Sahraoui, Optik - International Journal for Light and Electron Optics **128**, 8 (2017).
[13] M. Shkir, V. Ganesh, S. AlFaify, I. Yahia, and H. Zahran, Journal of Materials Science: Materials in Electronics **29**, 6446 (2018).